Modeling, Design, and Fabrication of High-Inductance Bond Wire Microtransformers With Toroidal Ferrite Core

Enrico Macrelli, Aldo Romani, Ningning Wang, *Member, IEEE*, Saibal Roy, *Member, IEEE*, Mike Hayes, Rudi Paolo Paganelli, Cian Ó Mathúna, *Fellow, IEEE*, and Marco Tartagni, *Member, IEEE*

***Abstract*—This paper presents the design of miniaturized bond wire transformers assembled with standard IC bonding wires and NiZn and MnZn ferrite toroidal cores. Several prototypes are fabricated on a printed circuit board substrate with various layouts in a $4.95\ \mathrm{mm} \times 4.95\ \mathrm{mm}$ area. The devices are modeled by analytical means and characterized with impedance measurements over a wide frequency range. Experimental results on 1:38 device show that the secondary self-inductance increases from 0.3 μH with air-core to 315 μH with ferrite core; the coupling coefficient improves from 0.1 with air-core to 0.9 with ferrite core; the effective turns ratio enhances from 0.5 with air-core to 34 with ferrite core. This approach is cost effective and enables a flexible design of efficient micromagnetics on top of ICs with dc inductance to resistance ratio of 70 μH/Ω and an inductance per unit area of 12.8 μH/mm^2 up to 0.3 MHz. The design targets the development of bootstrap circuits for ultralow voltage energy harvesting. In this context, a low-voltage step-up oscillator suitable for thermoelectric generator sources is realized with a commercial IC and the proposed microtransformers. Experimental measurements on a discrete prototype report that the circuit bootstraps from voltages down to 260 mV and outputs a dc voltage of 2 V.**

***Index Terms*—Bonding processes, converters, energy harvesting (EH), ferrites, magnetic cores, oscillators, permeability, power supply in package (PwrSiP), power supply on chip (PwrSoC), printed circuits, thermoelectric, transformers.**

I. Introduction

THE research community is currently devoting significant efforts in developing high-performance miniaturized magnetic components compatible with integrated circuit (IC) processes. In general, air-core inductors and planar transformers shaped as spirals are directly implementable in standard IC technologies, although with common difficulties in attaining good efficiencies and high inductance values.

Manuscript received December 20, 2013; revised September 5, 2014; accepted November 3, 2014. Date of publication November 13, 2014; date of current version May 22, 2015. This work was supported in part by the European Community's FP7 2007-2013 under Grant agreement Nanofunction no. 257375 and by the ENIAC-JTI under Grant agreement LAB4MEMs 325622. Recommended for publication by Associate Editor C. R. Sullivan.

E. Macrelli, A. Romani, and M. Tartagni are with the Advanced Research Center on Electronic Systems, University of Bologna, Cesena I-47521, Italy (e-mail: enrico.macrelli@unibo.it; aldo.romani@unibo.it; marco.tartagni@unibo.it).

N. Wang, S. Roy, M. Hayes, and C. Ó Mathúna are with the Tyndall National Institute, University College Cork , Cork Ireland (e-mail: ning.wang@tyndall.ie; saibal.roy@tyndall.ie; michael.hayes@tyndall.ie; cian.omathuna@tyndall.ie).

R. P. Paganelli is with the National Research Council CNR-IEIIT, University of Bologna, Bologna I-40136, Italy (e-mail: rudipaolo.paganelli@cnr.it).

Color versions of one or more of the figures in this paper are available online at http://ieeexplore.ieee.org.

Digital Object Identifier 10.1109/TPEL.2014.2370814

In fact, the overall size reduction of magnetic components is a strategic issue, as well as the minimization of the related power losses. The ultimate market drivers are pushing the growth of new miniaturized technologies referred to as power supply in package (PwrSiP) and power supply on chip (PwrSoC). In PwrSiP, magnetics are copackaged with the converter circuitry, whereas in PwrSoC, magnetics are integrated and, possibly, lead to the realization of monolithically integrated power supplies. However, on-chip magnetics usually require complex and expensive deposition techniques which currently limit their market use [1]. Another application area of miniaturized magnetics is the development of energy harvesting (EH) systems. In this field, silicon integration allows us to design advanced power conversion and management circuits in a very small footprint area of few square millimeters [2], [3]. In this type of applications, besides for power conversion, miniaturized magnetics are used as building blocks of low-voltage bootstrap circuits. However, external inductors or transformers are not usually shrinked correspondingly to silicon. Package level or on-chip integration of suitable magnetic components would ease the deployment of highly miniaturized autonomous systems.

In general, the main goals in the design of power converters are high efficiency and reduced power losses [1], [4]. In order to design highly efficient dc/dc converters, active semiconductor devices (i.e., MOSFETs) are used as switches, while reactive components (i.e., capacitors, inductors, and transformers) are required for temporarily storing energy and for filtering the periodic waveforms of the switching power converters, thus extracting the desired dc component. As a matter of fact, the quality factor of reactive elements significantly affects power dissipation losses. A present challenge for the miniaturization of switching power converters is the integration of passive components achieving similar performance of external discretes with a comparable footprint area in a frequency range between 0.5 and 10 MHz [1]. Recent advances in increasing the switching frequency in commercial step-up converters [5] have enabled the use of smaller passive components with lower inductances. However, such improvement is restricted by structural limitations of magnetic materials related to magnetic saturation and internal power losses [4], [5].

Power inductors and transformers are normally fabricated by winding a coil around a planar core as in solenoidal and toroidal structures, or by enclosing the coils within a multilevel magnetic core as in spirals [1]. The design of such devices must consider the current flowing in the coil which produces the magnetic field

in which energy is stored. A good microinductor should achieve a high inductance along with a low series resistance in a small area. In case a magnetic core is used, the inductance increases proportionally to the relative permeability of the core. However, a high permeability can lead to core saturation even for low values of the applied magnetic field, and to high ac core losses [1], [4]. In order to pursue miniaturization, various examples of devices with a magnetic core have recently been developed with microelectromechanical system (MEMS)-oriented fabrication processes compatible with silicon technology for PwrSoC and PwrSiP with toroidal or solenoid and spiral structures [6]–[11]. At very high frequencies, i.e., ≥40 MHz, small-sized air-core inductors with low inductances are generally an acceptable solution [4]; however, they present higher power losses in coils due to Joule effect with respect to magnetic core inductors, as many more turns are required to achieve a sufficient inductance. These aspects are clarified in [12], where a comparison between 36 nH magnetic- and air-core spiral inductors designed to operate up to 100 MHz is reported, with the conclusion that the performance of the magnetic core inductor is superior up to 50 MHz. However, for higher frequencies, additional fabrication steps, e.g., core lamination, are required to limit eddy-current power losses. Hence, in order to limit losses and increase efficiency, on-chip magnetic components require a magnetic core with accurate tuning in terms of geometries and materials.

Concerning the integration of inductors and transformers at wafer, package and board level, several techniques are available [13]. For package level integration, the magnetics are usually copackaged side by side with the die and connected within the package, whereas for wafer level integration, the magnetics are directly built on-chip, or on-top of the chip, thus decreasing the overall device area. The use of IC bonding wires based on solid-phase welding to enclose a magnetic core is a simple approach to form power devices, often called bond wire magnetics. A few examples of solenoid bond wire components have been reported in the literature [14]–[19], with permalloy and ferrite cores for use in the megahertz range. An interesting example of toroidal bond wire transformer has been reported in [17] with inductance close to 29 μH up to 1 MHz and above, with ferromagnetic low-temperature cofired ceramic (LTCC) as a magnetic core. Bond wire magnetics have several advantages compared to MEMS technology as a postprocessing step to fabricate the magnetics [14], [15]: above all the standard fabrication process, then the low resistivity of bonding wires compared to metallic thin films, and finally the high achievable quality factor which enables the realization of efficient switching power converters. These structures are also suitable for integration into the PwrSiP and PwrSoC platforms, with adjustable performance by varying wire loop height and core thickness. Besides, bond wire magnetics with toroidal core facilitate high inductance to dc resistance ratios, which is a key parameter to evaluate the dc performance of magnetics, as well as a small area [1], [4], [9]. In addition, a toroidal geometry produces a small external magnetic field over the active IC due to its planar closed magnetic path [20]–[22], which leads to lower circuit noise.

This paper presents a cost-effective approach for realizing bond wire transformers or inductors with multiple windings by using conventional gold IC bonding wires and soft ferrite cores. The components are designed to be used in step-up oscillators starting autonomously from very low input voltages, e.g., bootstrap circuits, in EH applications where the main switching converter starts to operate as soon as an overthreshold voltage is achieved. More specifically, the paper shows a design method and a fabrication technique for bond wire transformers with NiZn and MnZn ferrite cores and demonstrates how this technique is suitable for integration of magnetics built on-top of the active IC. With respect to the current state of the art for micromagnetics with toroidal and solenoid magnetic core, which is summarized in Table I, this study develops devices suitable for operation in the megahertz frequency range with the highest inductance and the highest turns ratio in such a range of frequency. Finally, in order to validate the proposed design, the paper also reports, as a case study, the implementation of a low-voltage step-up oscillator based on the LTC3108 IC for micropower EH applications. This paper is structured as follows. Section II shows the basic magnetic relationships used for analyzing and modeling the toroidal microtransformers. The dc inductance analysis is illustrated, and then, saturation, high-frequency effects, and power losses are described. Section III reports the bonding wire tests together with the design and fabrication details of the devices integrated on a printed circuit board (PCB) substrate. The assembly of different magnetic devices based on standard IC bonding wires is illustrated and the modeling results are presented. Section IV describes the measurement procedure together with the experimental results. Section V illustrates the implementation of a discrete low-voltage step-up oscillator with the designed transformers. Finally, the conclusions in Section VI are presented.

II. Basic Analysis

In this section, the basic magnetic relationships are discussed in order to model analytically the two-winding bond wire transformer. Initially, the toroidal structure and the dc design are presented. Then, the saturation and ac design with the series complex permeability model are analyzed, together with the evaluation of the power losses.

A. Toroidal Model and DC Design

The devices presented in this paper have a toroidal structure with bonding wires as coils and a soft ferrite as magnetic core. Fig. 1 depicts the two-winding transformer structure. Loops around the magnetic core are performed with bonding wires and completed on the underlying metallization layer. The toroidal transformer can be represented as a finite length solenoid closed on itself to form a toroidal shape with rectangular cross section [23]. The dc self-inductances of both windings ${L_{11}}^{\mathrm{DC}}$ and ${L_{22}}^{\mathrm{DC}}$ are estimated by the reluctance method as follows:

$$L^{\mathrm{DC}} = \frac{\mu_0 \mu_{rc} n^2 A_c}{l_c} = \frac{\mu_0 \mu_{rc} n^2 t_c (D_o - D_i)}{\pi (D_o + D_i)} \qquad (1)$$

where n is the number of turns of the side considered, $\mu_0 = 4\pi \times 10^{-7}$ H/m is the free-space permeability, μ_{rc} is the low-frequency core relative permeability, $A_c = t_c(D_o - D_i)/2$ is

TABLE I
COMPARISON OF DEVICES WITH TOROIDAL AND SOLENOID MAGNETIC CORE

Work	Device	Structure	Winding Technology	Magnetic Core Material	Max Inductance	Number of Turns	Max Q factor	Max Working Frequency
[14]	Transformer	Solenoid	Wire bonding	MnZn	70 nH	2 : 1	n.a.	300 MHz
[10]	Inductor	Solenoid	Electroplating	CoTaZr film	70.4 nH	17	6	10 MHz
[15]	Inductor	Solenoid	Wire bonding	MnZn	0.34 μH	10	28	5 MHz
[16]	Inductor	Solenoid	Wire bonding	Ferrite epoxy	0.45 μH	3	n.a.	5 MHz
[9]	Inductor	Toroidal	Electrochemical deposition	NiFe alloy	0.5 μH	12	20	10 MHz
[6]	Inductor	Toroidal	Flip-chip bonding	NiFe alloy	1.11 μH	33	8	1 MHz
[19]	Inductor	Toroidal	Wire bonding	Permalloy and ferrite	2.7 μH	35	n.a.	1 MHz
[17]	Transformer	Toroidal	Wire bonding	Magnetic LTCC†	29 μH	1:50	11.6	5–10 MHz
This work	Transformer	Toroidal	Wire bonding	NiZn and MnZn	315 μH*	1:38	24.5*	1–2 MHz

n.a.: data not available. †: low-temperature co-fired ceramic. *: at small-signals.

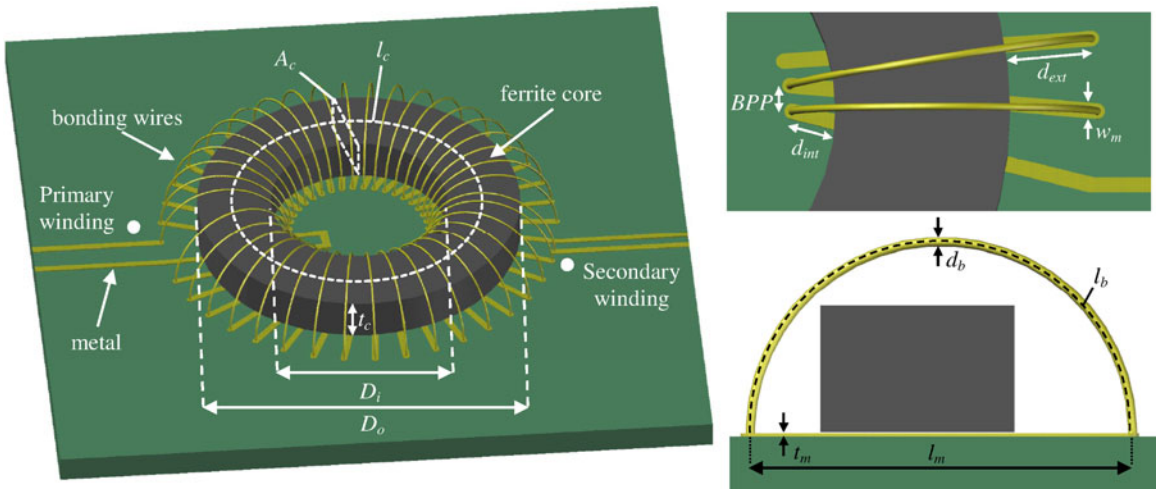

Fig. 1. Structure of the bond wire transformer with toroidal ferrite core and round bonding wires. Dimensions and design parameters are included.

the cross-sectional area of the core through which the magnetic flux flows, $l_c = \pi(D_o + D_i)/2$ represents the mean magnetic path length (MPL) which is the average length of the closed path followed by the magnetic flux within the core, D_o and D_i are the outer and inner diameters of the toroidal core, and t_c is the core thickness.

The dc series resistances of both windings R_{w1}^{DC} and R_{w2}^{DC} are obtained by summing the dc resistances of a single round bonding wire R_b^{DC} and of a single PCB rectangular metallization R_m^{DC} multiplied by the number of turns as

$$R_w^{\mathrm{DC}} = n(R_b^{\mathrm{DC}} + R_m^{\mathrm{DC}}) = n\left(\frac{\rho_b l_b}{\pi(d_b/2)^2} + \frac{\rho_m l_m}{w_m t_m}\right) \quad (2)$$

where ρ_b and ρ_m are the bonding wire and metallization resistivities, d_b is the wire diameter, l_b and l_m are the one-turn mean wire and metallization lengths, whereas w_m and t_m are the conductor width and thickness. It is also worth to recall that generally the flux produced by the primary winding is not entirely coupled to the secondary coil. Hence, in order to deal with this leakage, we define the mutual inductance L_{12} for any frequency by

$$L_{12} = k\sqrt{L_{11}L_{22}} \quad (3)$$

where k $(0 \le k \le 1)$ is the coupling coefficient, which measures the magnetic coupling between the coils, whereas L_{11} and L_{22} are the self-inductances. For the two-winding transformer sharing a common flux path, the turns ratio n_{12} is defined by

$$n_{12} = \frac{n_2}{n_1} \quad (4)$$

where n_1 and n_2 are the number of turns of primary and secondary side, respectively. In order to get the voltages over the windings, the effective turns ratio n_e is expressed as

$$n_e = k\sqrt{\frac{L_{22}}{L_{11}}}. \quad (5)$$

With a perfectly coupled transformer ($k \approx 1$), the effective turns ratio would become $n_e \approx n_{12}$, while (1) gives more exactly the self-inductances of the coils [23].

B. Saturation and AC Design

The relationship between the magnetic flux density B and the magnetic field intensity H is given by $B = \mu H$. The overall permeability $\mu = \mu_0\ \mu_{rc}$ describes how easily a material is magnetized. In order to prevent core saturation, the ampere-turn

limit for a transformer [23] should be taken into account

$$(n_1 I_1 + n_2 I_2) \leq I_{\max} = \frac{B_s l_c}{\mu} \tag{6}$$

where B_s is the saturation flux density corresponding to a complete alignment of the magnetic moments, $I_{\max}$ is the equivalent saturation current, while I_1 and I_2 are the amplitudes of the currents flowing in the primary and secondary coil, respectively. Additionally, I_1 and I_2 are recommended to comply with the current-carrying capability of a bonding wire according to the modified Preece equation [24]. From the saturation point of view, by considering a sinusoidal waveform applied to the primary winding with a peak amplitude $V_{1\max}$ and the secondary open, the minimum frequency $f_{\min}$ which prevents core saturation is given by

$$f_{\min} = \frac{V_{1\max}}{2\pi n_1 A_c B_s}. \tag{7}$$

At higher frequencies, the current flowing in a coil induces a magnetic field thus producing the well-known skin effect in the conductor. Hence, the current tends to circulate near the surface causing the current density to decrease from the top to the center of the conductor. In this analysis, the proximity effect produced by magnetic field induced by currents flowing in nearby conductors is neglected. The frequency behavior of the windings is analyzed through the skin depth in bonding wires δ_b defined as

$$\delta_b = \sqrt{\frac{\rho_b}{\pi \mu_0 \mu_{rb} f}} \tag{8}$$

where μ_{rb} is the bonding wire relative permeability. The skin effect in the bonding wire is negligible only if $\delta_b >> d_b$. Similarly, a time-varying magnetic field in a magnetic core induces a voltage which produces circulating currents in the same core. These currents follow circular paths normal to the direction of the magnetic flux and produce a secondary magnetic field which opposes the original applied magnetic field. Hence, the frequency behavior of a conductive core depends also on the core skin depth δ_c as

$$\delta_c = \sqrt{\frac{\rho_c}{\pi \mu_0 \mu_{rc} f}} \tag{9}$$

where ρ_c is the core resistivity. The skin effect in the core is negligible only if $\delta_c >> t_c$. Usually, soft ferrites satisfy this condition due to the high resistivity. Considering the above equations, the ac resistances of the windings R_{w1} and R_{w2} are then obtained by summing the ac resistances of a single round bonding wire R_b and of a single rectangular metallization R_m multiplied by the number of turns as

$$R_w = n(R_b + R_m) = n\left(\frac{\rho_b l_b}{\pi \delta_b (d_b - \delta_b)} + \frac{\rho_m l_m}{2\delta_m w_m}\right) \tag{10}$$

where δ_m is the metallization skin depth obtained from (8) by considering the PCB metal characteristics.

Since the permeability at high frequencies becomes a complex quantity, it can be used to represent all types of core losses, specifically for soft ferrites [23]. This will be applied herein for deriving a small-signal model useful for comparison with small-signal measurements performed in Section IV. The series complex permeability μ_s of a magnetic core is given by

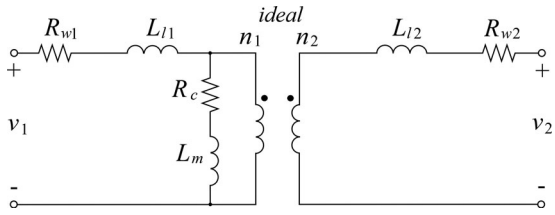

Fig. 2. Equivalent circuit model of the transformer referred at the primary side with nonperfect coupling and losses.

$$\mu_s = \mu_s' - i\mu_s'' = \mu_0(\mu_{rs}' - i\mu_{rs}'') \tag{11}$$

where μ_s' is the inductive permeability, μ_s'' is the resistive permeability, μ_{rs}' is the inductive relative permeability, and μ_{rs}'' is the resistive relative permeability. Based on the above concerns, the small-signal ac self-inductances L_{11} and L_{22} are approximated with the series complex permeability model as

$$L = L_0^{\mathrm{DC}} \mu_{rs}' \approx \frac{\mu_0 \mu_{rc} n^2 A_c}{l_c \sqrt{1 + (f/f_H)^2}} \tag{12}$$

where L_0^{DC} is the dc self-inductance obtained from (1) with $\mu_{rc} = 1$, and f_H is the -3-dB frequency of the μ_{rs}' characteristic provided by the producer of core material (or estimated from measurements). In order to characterize the ac core losses, the small-signal core equivalent series resistance R_c is approximated by

$$R_c = 2\pi f L_0^{\mathrm{DC}} \mu_{rs}'' \approx \frac{2\pi f \mu_0 \mu_{rc} n^2 A_c}{l_c \sqrt{1 + Q^2 (f/f_H - f_H/f)^2}} \tag{13}$$

where $Q = f_H/\Delta f$ is the quality factor with Δf as the -3-dB bandwidth of the μ_{rs}'' characteristic provided by the manufacturer (or estimated). Finally, the small-signal ac series resistances of both sides R_{11} and R_{22} are modeled by

$$\begin{aligned} R_{11} &= R_{w1} + R_c \\ R_{22} &= R_{w2} + R_c n_{12}^2. \end{aligned} \tag{14}$$

Fig. 2 shows the equivalent transformer circuit referred at the primary side with $L_{l1} = L_{11}(1-k)$ and $L_{l2} = L_{22}(1-k)$ as the leakage inductances and $L_m = kL_{11}$ as the magnetizing inductance.

C. Power Losses

In order to evaluate the large-signal performance in a power application, the ac power losses in the core P_c (mW), due to both eddy-current and hysteresis losses, are estimated by the classical Steinmetz equation [4], [5]

$$P_c = k_c f^a B_m^b V_c \tag{15}$$

where k_c, a, and b are the core loss constants, f (kHz) is the operating frequency, B_m (G) is the amplitude of the ac component of the magnetic flux density, and $V_c = A_c\, l_c$ (cm^3) is the core

volume. Besides, the ac power losses in the windings P_w (W) are estimated by

$$P_w = R_{w1} I_{1\mathrm{rms}}^2 + R_{w2} I_{2\mathrm{rms}}^2 \tag{16}$$

where $I_{1\mathrm{rms}}$ and $I_{2\mathrm{rms}}$ are the rms values of I_1 and I_2.

III. Design and Fabrication

This section describes the bonding wire tests and the fabrication details of the layout designed on a PCB substrate. The assembly of the prototypes is also discussed together with the modeling results.

A. Bonding Wire Tests

A Kulicke & Soffa (K&S) 4524 gold wire bonder with thermosonic ball-wedge bonding is used to enable closer wire placement [25], [26] thus leading to the realization of high turns ratio devices. Crucial design parameters in terms of bonding wires include wire diameter, material, and minimum spacing [15], [27]. Gold round wires are chosen for the low resistivity of gold ($\rho_b = 2.44 \times 10^{-6}\ \Omega \cdot \mathrm{cm}$) which minimizes the resistance of the wires. Furthermore, a small spacing between wires, thanks to the ball-wedge bonding, enhances the self-inductances and the coupling coefficient. In order to analyze the wire bonder capability, several bond tests are performed with two different gold wire diameters and bond pad pitches *BPP* on a blank silicon substrate coated with gold with an epoxy mold mounted on top. The above quantities are depicted in Fig. 1. The performed bonds suggest that thick round wires ($d_b = 32\ \mu$m) are more robust and have smaller resistance (≈80 mΩ/bond) with BPP ≅ 130 μm. Meanwhile, thin round wires ($d_b = 25\ \mu$m) are less robust and more resistive (≈130 mΩ/bond) due to their smaller diameter, even if allowing lower BPP ≅ 112 μm. As a result, gold thick round wires are chosen as the best choice to design robust devices.

B. Design on PCB Substrate

The prototypes are designed on a single-layer PCB (370HR material, 0.33 mm thick) with thin and ultranarrow copper conductor ($t_m \approx 15\ \mu$m, $\rho_m = 1.68 \times 10^{-6}\ \Omega \cdot \mathrm{cm}$) plus a nickel–gold finish fabricated by Litho-Circuits. The transformer design is based on several parameters that can in perspective be optimized jointly. However, the requirements of our application impose some characteristics: the largest turns ratio n_{12} and self-inductances L_{11}, L_{22} are highly desirable in order to get the bootstrap oscillator started with the minimum supply voltage. Therefore, although a full optimization of parameters is not performed, following these targets, four layouts are designed in a footprint area of $A_r = 4.95\ \mathrm{mm} \times 4.95\ \mathrm{mm}$ (fixed by the adopted ferrite cores), with different configurations of the PCB parameters such as conductor width w_{m} and minimum spacing s_{min}, and wire bonder constraints such as BPP and outer-inner d_{ext}, d_{int} pad distances from the magnetic core.

The first layout, indicated as T_1, is designed with the smallest and narrowest metallizations allowed by the used technology, thus maximizing n_{12}. The second layout, indicated as T_2, is designed with larger and wider metallizations in order to provide a higher yield in the wire bonding process. The third layout, indicated as T_3, is designed with a wider d_{int}, therefore admitting more space for the capillary insertion and permitting the assembly of thicker cores, however reducing n_2. The last layout, indicated as T_4, is similar to T_1 but with $n_1 = 2$ in order to improve k and L_{11}. Fig. 1 on the top right shows the geometrical parameters and constraints for the design of the toroidal devices. Table II reports a summary of the transformer layouts characteristics designed on the PCB substrate. A full design optimization, according also to the properties of external circuits, should include the choice of combining series and parallel connections of bonding wires to increase the inductance and reduce the resistance.

TABLE II
Summary of the Transformer Layouts Characteristics on PCB Substrate

Layout	$n_1 : n_2$	w_{m} (μm)	s_{min} (μm)	BPP (μm)	$d_{\mathrm{ext}}, d_{\mathrm{int}}$ (μm)
T_1	1:38	80	50	130	450, 225
T_2	1:33	90	60	150	450, 225
T_3	1:28	90	70	160	450, 300
T_4	2:35	80	50	130	450, 225

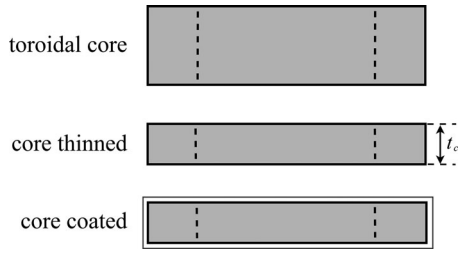

Fig. 3. Thinning and coating steps of the toroidal ferrite cores.

C. Magnetic Ferrite Cores

The main design parameters related to the magnetic core include core thickness and permeability [15]. Several miniaturized high-permeability toroidal ferrites are investigated as magnetic core to increase the inductance and improve the coupling of the micromagnetics. The first part is Fair-Rite 5943000801 which is a NiZn (43 material) toroid with high resistivity. The second part is Fair-Rite 5975000801 which is a MnZn (75 material) toroid with high relative permeability. The third part is Epcos B64290P36X830 which is a MnZn (N30 material) toroid with high relative permeability. Finally, an epoxy mold core ($\mu_{rc} = 1$) with the same dimension is used to evaluate the improvements obtained by the insertion of a magnetic core. The use of a dummy core provides also mechanical support for the wires instead of just air.

Although miniaturized ferrites are available in commerce, IC packages and wire bonder capillaries impose restrictions on the maximum core thickness t_{c} practicable [4], [27]. Hence, the ferrites are first thinned and then coated in laboratory. During thinning, t_c is reduced with a polishing machine to allow the wire bonder capillary to reach the inner pads

TABLE III
ELECTRICAL AND MAGNETIC PROPERTIES OF THE TOROIDAL FERRITES AND DUMMY CORE

Supplier	Part Number	Material	$D_o \times D_i \times t_c$ (mm)	μ_{rc}	ρ_c ($\Omega \cdot$ cm)	H_c (A/m)	B_s (mT)	B_r (mT)	k_c, a, b @100°C $f =$ 0.1 MHz	f_H, Δf (MHz)
Fair-Rite	5943000801	NiZn 43	$3.95 \times 2.15 \times 0.47$	800	10^5	35.8	290	130	n.a.	15, 23
Fair-Rite	5975000801	MnZn 75	$3.95 \times 2.15 \times 0.42$	5000	3×10^2	12.7	430	140	6.6×10^{-8}, 1.52, 2.19	0.8, 1.7
Epcos	B64290P36X830	MnZn N30	$4.00 \times 2.40 \times 0.50$	4300	0.5×10^2	12.0	380	n.a.	n.a.	0.9, 2.0
n.a.	Dummy mold	Epoxy	$3.92 \times 2.12 \times 0.50$	1	n.a.	n.a.	n.a.	n.a.	n.a.	n.a.

n.a.: data not available.

of the device. However, t_c can be further reduced if necessary for an IC implementation, hence decreasing the self-inductances and reducing the core losses. During coating (performed only on the MnZn 75 core), the thinned core is coated with an insulation film to prevent any conductive paths between core and coils. Fig. 3 shows the thinning and coating steps of the ferrites. The electrical and magnetic properties of the isotropic magnetic cores are summarized in Table III, with B_r as the residual flux density (or remanence) which represents the remnant magnetization for $H = 0$ A/m, and H_c as the core coercivity which denotes the magnetic field intensity required for reducing the flux density to $B = 0$ T.

D. Assembly of Devices

The ferrite cores are assembled to the PCB substrate and bonded with a K&S 4524 gold wire bonder from inner to outer pads in a clean room environment, thus obtaining sixteen different prototypes: four cores $\times$ four layouts. The devices are realized with the bonder in manual mode with a full control of the bonding head and a work-holder temperature of about 100 °C. However, automatic bonding can also be used to assembly the devices [25]. Fig. 4 illustrates four pictures of each core assembled with thick gold bonding wires and various layouts: T_1 layout (1:38) with NiZn 43 core (top left), T_2 layout (1:33) with MnZn 75 core (top right), T_3 layout (1:28) with MnZn N30 core (bottom left), and T_4 layout (2:35) with epoxy core (bottom right). Since our target is the development of a low-voltage battery-less startup circuit for micropower harvesting applications, we choose $1 : n_2$ or $2 : n_2$ turns in order to achieve a high voltage ratio for testing purposes and for giving the possibility of fabricating inductors, i.e., with the only secondary coil, with the highest inductance value.

Since the chosen turn ratios are specific for the targeted application, this configuration is not optimal for typical power conversion applications. For future designs, the turns ratio and the winding resistances should be adapted for the desired power application, for instance, by using more bonding wires in parallel for the primary and in series for the secondary, in order to account for different levels of current. After the assembly, the devices present approximately: reduced core thickness $t_c \cong 0.45$ mm, core cross section $A_c \cong 0.41$ mm^2, core mean MPL $l_c \cong 9.6$ mm, one-turn mean metallization length $l_m \cong 1.6$ mm, and one-turn mean wire length $l_b \cong 2.6$ mm.

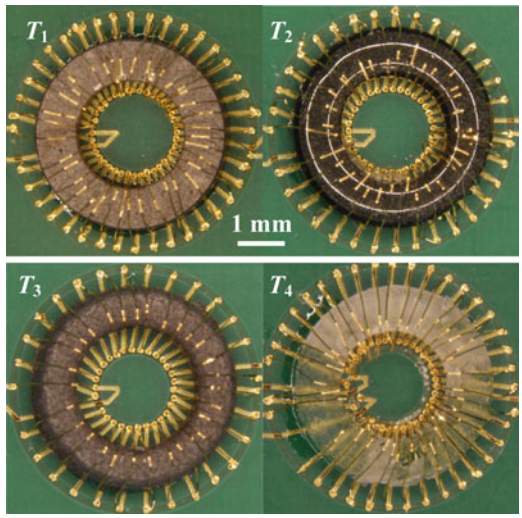

Fig. 4. Microphotographs of the devices assembled with thick gold bonding wires: T_1 layout (1:38) with NiZn 43 core (top left), T_2 layout (1:33) with MnZn 75 core (top right), T_3 layout (1:28) with MnZn N30 core (bottom left), and T_4 layout (2:35) with epoxy core (bottom right).

E. Modeling Results

The analytical performances of the transformers are analyzed by using the equations presented in Section II. The dc self-inductances L_{11}^{DC} and L_{22}^{DC} are estimated by (1), while the dc winding resistances R_{w1}^{DC} and R_{w2}^{DC} are obtained by (2). Table IV shows the modeling results of the dc self-inductances and winding resistances of the bond wire devices. L_{11}^{DC} of $T_{1\ldots3}$ layouts increases from 2.6 nH with epoxy core to 0.051 μH with NiZn 43 core. The other ferrites enable further increases from 0.051 to 0.255 μH with MnZn 75 core. L_{22}^{DC} of the T_1 layout increases from 0.21 μH with epoxy core to 60.8 μH with NiZn 43 core. The other ferrites enable further increments from 60.8 to 339 μH with MnZn 75 core. R_{w1}^{DC} of $T_{1\ldots3}$ layouts for all cores is 0.20 Ω, whereas for the T_4 layout is equal to 0.40 Ω for all cores due to the higher n_1. R_{w2}^{DC} ranges from 3.8 Ω for the T_1 layout to 2.7 Ω for the T_3 layout for all ferrites.

Besides this, the equivalent saturation current $I_{\max}$ is estimated by (6), while the minimum frequency to avoid saturation $f_{\min}$ is evaluated by (7). Finally, the large-signal ac power losses in the core P_c and windings P_w are estimated by (15) and (16). Table V shows the modeling results of the saturation, ac analysis, and power losses of the bond wire devices. $I_{\max}$ ranges from 2.76 A for the NiZn 43 core to 0.656 A for MnZn 75

TABLE IV
MODELING RESULTS OF THE DC SELF-INDUCTANCES AND WINDING RESISTANCES OF THE BOND WIRE DEVICES

	Core	NiZn 43	MnZn 75	MnZn N30	Epoxy
$L_{11}{}^{\mathrm{DC}}\,(\mu H)$ (1)	$T_{1\ldots3}$	0.051	0.255	0.222	2.6×10^{-3}*
	T_4	0.185	0.998	0.867	5.2×10^{-3}†
$L_{22}{}^{\mathrm{DC}}\,(\mu H)$(1)	T_1	60.8	339	294	0.21‡
	T_2	45.4	254	220	0.16‡
	T_3	32.4	181	157	0.11‡
	T_4	51.3	287	249	0.17‡
$R_{w1}{}^{\mathrm{DC}}\,(\Omega)$! (2)	$T_{1\ldots3}$	0.20	0.20	0.20	0.20
	T_4	0.40	0.40	0.40	0.40
$R_{w2}{}^{\mathrm{DC}}\,(\Omega)$ (2)	T_1	3.8	3.8	3.8	3.8
	T_2	3.2	3.2	3.2	3.2
	T_3	2.7	2.7	2.7	2.7
	T_4	3.5	3.5	3.5	3.5

*: inductance of a semi-circular loop of round wire as described in [23].
†: inductance of two semi-circular loops of round wires in series [23].
‡: estimated through (1) by considering $A_c \approx {l_b}^2/(2\cdot\pi) = 1.07$ mm^2.
!: comprises ≈0.1 Ω of resistance from device's terminals to PCB contacts.

TABLE V
MODELING RESULTS OF SATURATION, AC ANALYSIS, AND POWER LOSSES OF THE BOND WIRE DEVICES

	Core	NiZn 43	MnZn 75	MnZn N30	Epoxy
$I_{\max}$ (A) (6)	$T_{1\ldots4}$	2.76	0.656	0.707	-
$f_{\min}$ (kHz) (7)	$T_{1\ldots3}$	130	98	105	-
$V_{1\max} = 0.1$ V	T_4	65	49	52	-
P_c (mW) (15)					
$B_m = 10^3$ G	$T_{1\ldots4}$	n.a.	1.04	n.a.	-
$f =$ 100 kHz					
P_w (mW) (16)	T_1	0.26	0.26	0.26	0.26
$I_{1\mathrm{rms}} = 50$ mA	$T_{2\ldots3}$	0.25	0.25	0.25	0.25
$I_{2\mathrm{rms}} \cong I_{1\mathrm{rms}}/n_{12}$					
$f =$ 100 kHz	T_4	0.53	0.53	0.53	0.53

n.a.: data not available.

core for all layouts. In addition, the modified Preece equation provides a range of recommended maximum current in each coil from 0.665 to 0.970 A for gold wires with $d_b = 32$ μm and $l_b \cong 2.6$ mm [24]. $f_{\min}$ on the primary side with $V_{1\max} = 0.1$ V (which is the typical target for bootstrap circuits in our application) ranges from 130 kHz for the NiZn 43 core to 98 kHz for the MnZn 75 ferrite for $T_{1\ldots3}$ layouts, while for T_4 layouts, the values are half of those previous due to the double n_1. Besides, by considering a sinusoidal waveform applied on the secondary side of the T_1 layout with NiZn 43 core with peak amplitude $V_{2\max} = 2$ V (which is a sufficient output voltage for starting a conventional dc/dc converter in micropower EH applications), we obtain $f_{\min} = 68$ kHz. Finally, P_c with $B_m = 10^3$ $G = 0.1$ T at $f = 100$ kHz is equal to 1.04 mW for the MnZn 75 core and all layouts, whereas P_w by assuming for instance $I_{1\mathrm{rms}} = 50$ mA and thus $I_{2\mathrm{rms}} \cong I_{1\mathrm{rms}}/n_{12}$ at $f = 100$ kHz is equal to ≅0.25 mW for all devices except for T_4 layouts for which is ≅0.53 mW.

IV. IMPEDANCE MEASUREMENTS

This section describes the impedance characterization procedure performed on the devices and the measurement results obtained.

A. Measurement Procedure

The main parameters of the transformers are extracted from the two-port network by performing standard open and short circuit (SOS) tests as suggested in [23], [28], [29]. In SOS tests, the secondary coil is left open ($I_2 = 0$ A) while applying an ac voltage with frequency f_{ac} to the primary winding. Measurements at the primary terminals give the primary impedance $Z_{11} = R_{11} + i\ 2\pi\cdot f_{\mathrm{ac}} L_{11}$. Similarly, for the secondary coil, measurements provide the secondary impedance $Z_{22} = R_{22} + i\ 2\pi\cdot f_{\mathrm{ac}} L_{22}$.

In order to assess the coupling between the coils, the mutual inductance L_{12} is measured with series-coupling tests [29]. First, the two windings are connected in series-aiding mode with the two minus terminals short-circuited. Measurements at the two plus terminals give the series-aiding inductance $L_a = L_{11} + L_{22} + 2\cdot L_{12}$. Second, the two windings are connected in series-opposing mode with plus and minus terminals of different coils short-circuited. Measurements at the other terminals provide the series-opposing inductance $L_b = L_{11} + L_{22} - 2\cdot L_{12}$. Hence, the mutual inductance L_{12} is extracted as follows:

$$L_{12} = \frac{(L_a - L_b)}{4}. \tag{17}$$

The series-coupling tests combined with SOS tests can be used to compute the transformer parameters only if the magnetizing flux density is common for all tests. However, the differential impedance varies little with excitation current thus providing results with negligible errors [29]. Hence, k and n_e are extracted by (3) and (5), respectively. Finally, the quality factors Q_{11} and Q_{22} of both sides are given by the following expressions [4], [30]:

$$Q_{11} = \frac{2\pi f_{\mathrm{ac}} L_{11}}{R_{11}} \tag{18}$$

$$Q_{22} = \frac{2\pi f_{\mathrm{ac}} L_{22}}{R_{22}}. \tag{19}$$

The polarity of the mutual induced voltage depends on the way the coils are encircled in relation to the reference direction of coil currents, which are indicated by the dot convention [23] as shown in Fig. 1 on the left. Since the current I_1 flowing into the terminal of the primary produces a magnetic flux, the dotted terminal in the remaining coil is the one whose current I_2 generates a magnetic flux in the same direction. If both ac voltages V_1 and V_2 have the same polarity at the dotted terminal, the transformer is noninverting and its transfer function A_v is given by

$$A_v = \frac{V_2}{V_1} = \frac{I_1}{I_2}. \tag{20}$$

B. Measurement Results

Impedance measurements are performed by using precision E4980A and 4285A LCR Meters calibrated with open and short circuit tests (1 m cable length, single mode) to compensate the

parasitic reactance of cables, with an applied small ac voltage level set to 10-mV rms without bias, unless otherwise noted.

Fig. 5 on the left shows the comparisons between the calculated by small-signal model (12) and measured L_{11} and L_{22} of the device with NiZn 43 core for T_1 layout. The calculated L_{11} and L_{22} agree with measurements in the whole examined frequency range, with a maximum measured L_{22} of 63 μH. Fig. 5 on the right displays the comparisons between the calculated by small-signal model (14) and measured R_{11} and R_{22} of the device with NiZn 43 core for T_1 layout. Similarly, the calculated R_{11} and R_{22} adequately agree with measurements, whereas high-frequency effects (core losses) start to affect the device above $\cong$1–2 MHz. Fig. 6 on the left shows the measured k and n_e, whereas Fig. 6 on the right reports the measured Q_{11} and Q_{22} with (18) and (19), both of the devices with NiZn 43 core for all layouts. The results show that k is improved from $\cong$0.7 with T_3 to $\cong$0.9 with T_4, n_e is increased from $\cong$15.5 with T_4 to $\cong$27 with T_1, while maximum Q_{22} ranges from $\cong$12.5 at 0.5 MHz for T_2 to $\cong$19.5 at 0.5 MHz for T_1.

Fig. 7 shows the comparisons between the calculated and measured L_{11}, L_{22} (left) and R_{11}, R_{22} (right) of the device with MnZn 75 core for T_1 layout. The predicted L_{11} and L_{22} adequately match with measurements, as well as the calculated R_{11} and R_{22}, with a maximum measured L_{22} of 315 μH, greater than the previous NiZn 43 core due to the higher μ_{rc}. We observe that core losses start to influence the transformer from 0.5 MHz. Fig. 8 on the left displays the measured k and n_e, whereas Fig. 8 on the right reports the measured Q_{11} and Q_{22}, both of the devices with MnZn 75 core for all layouts. The results show that k is improved from $\cong$0.8 with T_2 to $\cong$0.9 with $T_{1,4}$, n_e is increased from $\cong$17 with T_4 to $\cong$34 with T_1, while peak Q_{22} ranges from $\cong$10 at 70 kHz for T_2 to $\cong$21.5 at 0.1 MHz for T_1.

Fig. 9 shows the comparisons between the predicted and measured L_{11}, L_{22} (left) and R_{11}, R_{22} (right) of the device with MnZn N30 core for T_1 layout. The calculated L_{11} and L_{22} almost coincide with measurements with a maximum measured L_{22} of 250 μH lower than the MnZn 75 core due to the lower μ_{rc}. The calculated R_{11} and R_{22} show an adequately match with measurements. Fig. 10 on the left presents the measured k and n_e, whereas Fig. 10 on the right demonstrates the measured Q_{11} and Q_{22}, both of the devices with MnZn N30 core for all layouts. The results show that k is equal to $\approx$0.95 for $T_{1\ldots4}$, n_e is increased from $\cong$17 with T_4 to $\cong$32 with T_1, and maximum Q_{22} ranges from $\cong$15.5 at 0.1 MHz for T_3 to $\cong$24.5 at 0.1 MHz for T_2.

In order to evaluate the benefits of a magnetic core, Fig. 11 reports the comparisons between calculated and measured L_{11}, L_{22} (left) and R_{11}, R_{22} (right) of the device with epoxy core for T_1 layout. The predicted L_{11} and L_{22} underestimate the measured values due to the high leakage inductances, while there are no ac effects in the examined frequency range. Besides, the calculated R_{11} and R_{22} almost coincide with measurements (the discrepancy is due to the contact resistance between metals and bonding wires). We remark that ferrite core devices provide a maximum up to 1000 times in L, 9 times in k, and 34 times in n_e compared to air-core devices. By comparing the right pictures of Figs. 5, 7, 9, and 11, we deduce that the increases of R_{11} and R_{22} in ferrite devices are attributed to both hysteresis and eddy-current losses in the core. This means that parasitic capacitances in the windings are negligible in the observed frequency range.

For a deeper characterization of the transformers at larger ac voltages typical for EH circuits, Fig. 12 illustrates the measured Q_{11}, Q_{22} (left) and L_{11}, L_{22} (right) of the device with MnZn 75 core and T_1 layout for different rms voltage levels: 10 mV, 0.1 V, and 1 V. The results show that for higher ac voltages, the peak Q_{22} decreases due to the growth of core losses, while Q_{11} does not vary appreciable. Besides, L_{22} at low frequencies increases for larger ac voltages, while L_{11} remains the same. We conclude that the performance of the MnZn device in such frequency range with signal amplitudes up to 1 V progressively degrades. In power conversion, the performance of a converter will be affected by the growth of core losses. A possible solution would be to decrease t_c, thus reducing the losses at the cost of lower inductances.

Finally, the transfer function A_v in (20) is extracted by applying an ac sinusoidal voltage with $f_{\rm ac} = 1$ MHz and peak-to-peak amplitude of 3.2 V at the primary coil by a function generator. Fig. 13 depicts the measured primary V_1 and secondary V_2 voltages of the MnZn N30 with T_2 (1: 33) layout achieved with a MSO 2024 Oscilloscope ($Z_L = 10$ MΩ). The primary peak-to-peak voltage is reduced to 150 mV due to the voltage partition between the internal resistance (50 Ω) of the function generator and Z_{11}. The measurement results demonstrate that the bond wire transformer does not exhibit distortion and boosts the primary voltage up to $A_v \cong 18$ with a secondary peak-to-peak voltage of about 2.7 V.

V. Low-Voltage Step-Up Oscillator for EH Applications

This section describes the target application of our preliminary design investigation. EH systems extract energy from the environment, store the energy, and supply it to low-power and low-voltage circuits. Thermoelectric generators (TEGs) provide a good solution for battery-less EH applications. TEGs with output voltages up to hundreds mV/K have been developed with microelectronic processes [31], which allow us to integrate high numbers of miniaturized thermocouples with overall electrical resistances in the order of hundreds Ω. However, micropower TEGs generally deliver low-voltage outputs in the range from 10 to 50 mV/K and present very low resistances usually lower than 1 Ω. Hence, for industrial or body applications with a temperature gradient of 6 K between hot and cold side, the expected output voltage is lower than 300 mV, thus smaller than the threshold voltage of diodes or transistors. As a consequence, it would be difficult or impossible to directly supply a conventional boost converter or a charge pump. Hence, in order to design battery-less systems, specific low-voltage step-up converters are required to take advantage of the low voltage available from TEGs. These circuits bootstrap the electronic system from fully discharged states and produce functional higher output voltages suitable to control semiconductor devices. Since this type of circuits targets the lowest possible start-up voltage

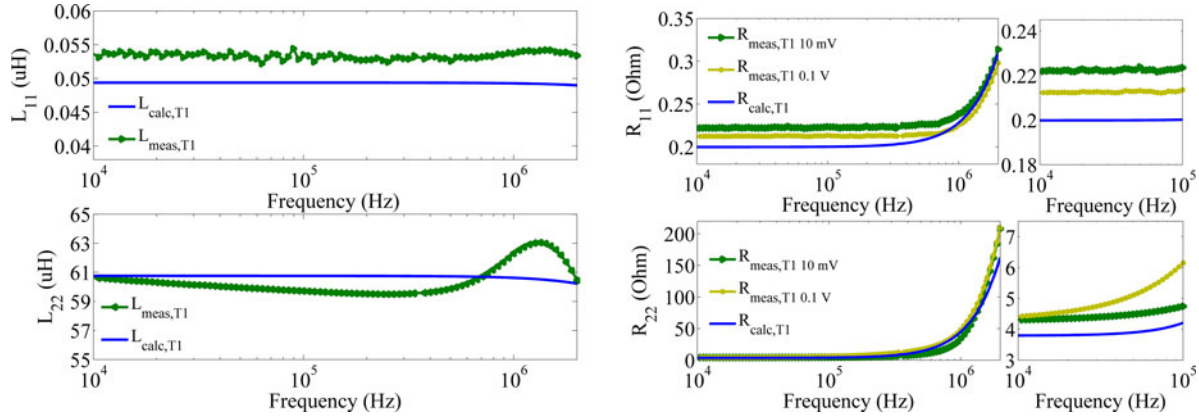

Fig. 5. Comparisons between predicted and measured L_{11}, L_{22} (left) and R_{11}, R_{22} (right) of the device with NiZn 43 core for T_1 layout.

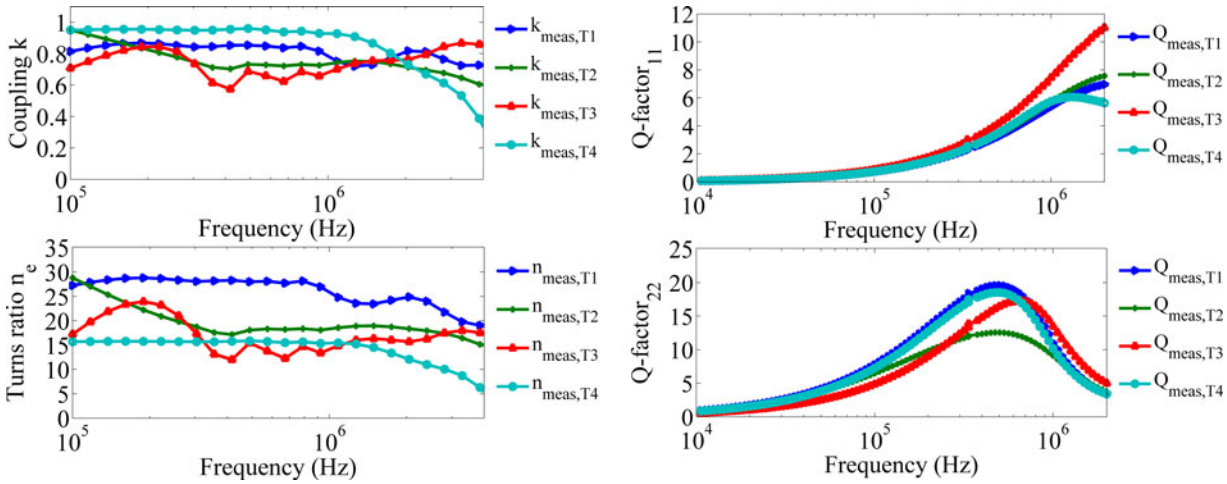

Fig. 6. Measured k, n_e (left) and Q_{11}, Q_{22} (right) of the devices with NiZn 43 core for $T_{1\ldots4}$ layouts.

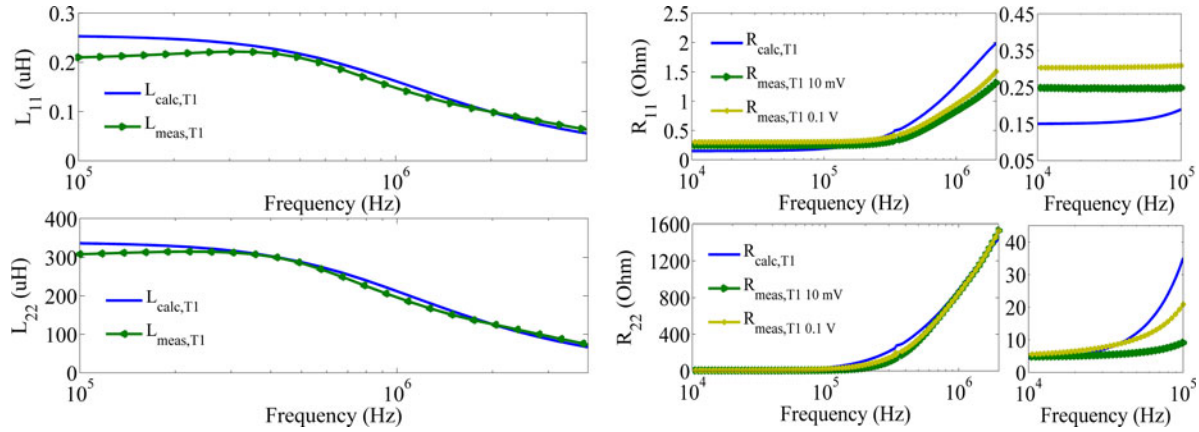

Fig. 7. Comparisons between predicted and measured L_{11}, L_{22} (left) and R_{11}, R_{22} (right) of the device with MnZn 75 core for T_1 layout.

rather than conversion efficiency, once this higher voltage is generated, a conventional power converter can be activated for transferring power from the TEG.

Analog step-up converters have been proposed in the state of the art using TEG sources [32], [33], with the startup circuit realized separately from the main power conversion block. Several solutions for low-voltage circuits are also present in the market such as the LTC3108 [34] IC from Linear Technology. This converter uses a normally-ON MOSFET and a resonant oscillator scheme with an external step-up transformer (e.g., [35] and [36]) to convert from ultralow input voltage. Additionally, it can operate with different types of voltage sources such as TEGs,

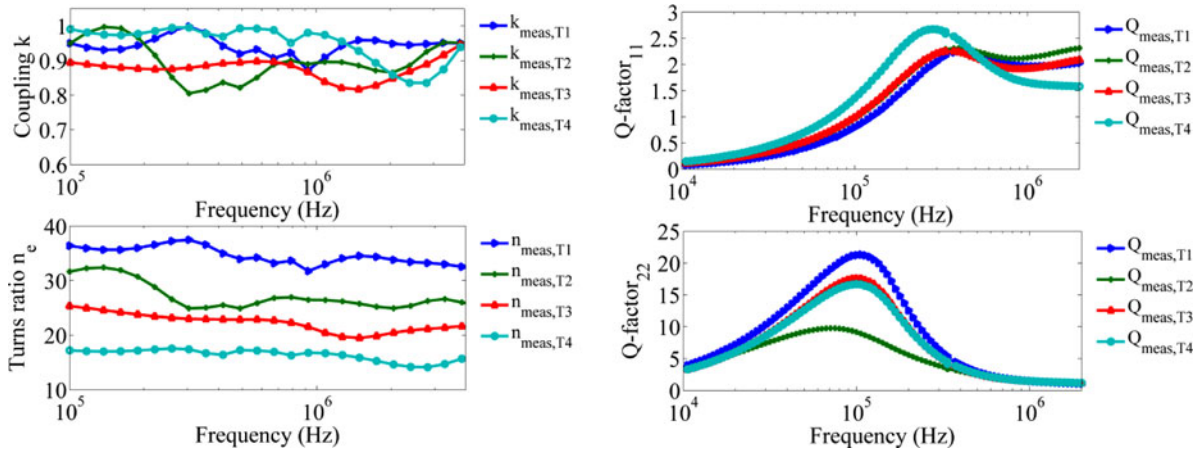

Fig. 8. Measured k, n_e (left) and Q_{11}, Q_{22} (right) of the devices with MnZn 75 core for $T_{1\ldots4}$ layouts.

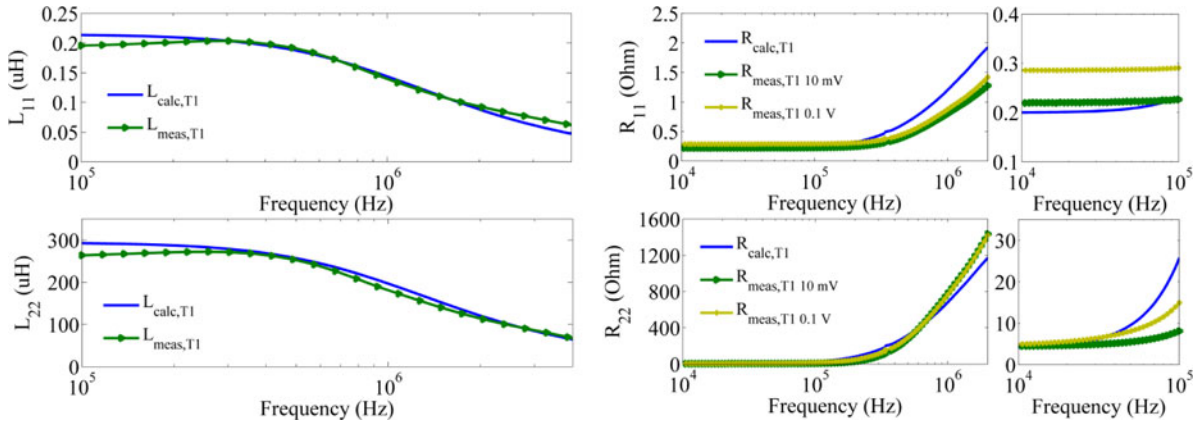

Fig. 9. Comparisons between predicted and measured L_{11}, L_{22} (left) and R_{11}, R_{22} (right) of the device with MnZn N30 core for T_1 layout.

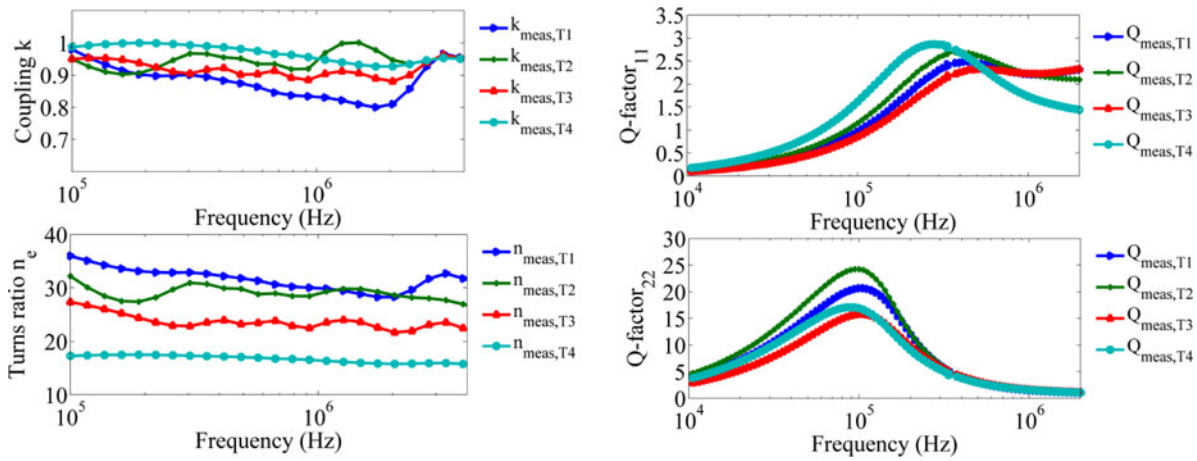

Fig. 10. Measured k, n_e (left) and Q_{11}, Q_{22} (right) of the devices with MnZn N30 core for $T_{1\ldots4}$ layouts.

thermopiles, and photovoltaic cells. In the following measurements, we only focus on the step-up oscillator and deactivate all the remaining subcircuits (such as LDO, etc.).

For validating the proposed micromagnetics, the bond wire MnZn N30 device with T_4 (2:35) layout is chosen due to the higher L_{11} as step-up transformer. Similarly, an LPR4012–202LML [36] Coilcraft transformer (1:10) with comparable performance is used for comparison purposes. Fig. 14 depicts the circuit diagram of the step-up oscillator based on the LTC3108 IC with the microtransformer included. Specified pin functions are indicated in the figure caption. A discrete prototype is realized with a filter capacitor $C_{\text{in}} = 220$ μF, a pump capacitor

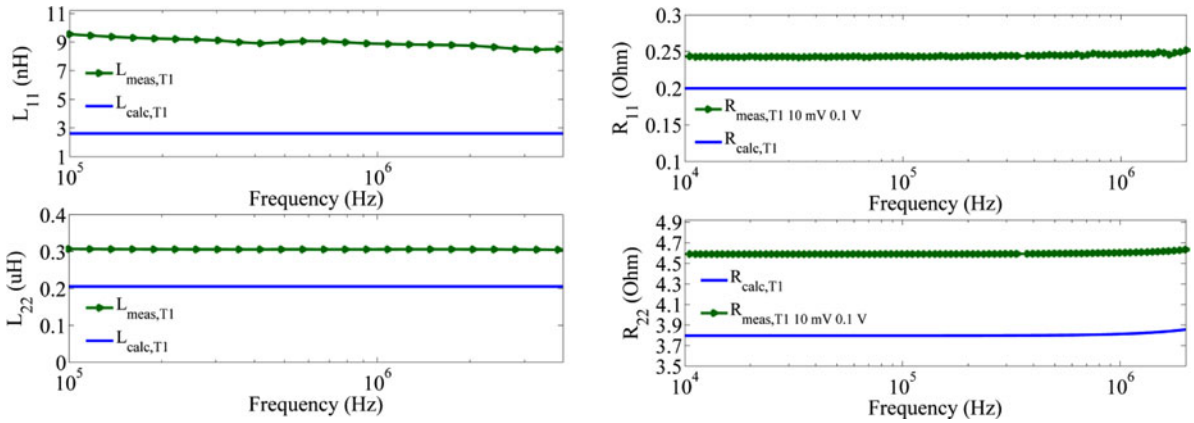

Fig. 11. Comparisons between predicted and measured L_{11}, L_{22} (left) and R_{11}, R_{22} (right) of the device with epoxy core for T_1 layout.

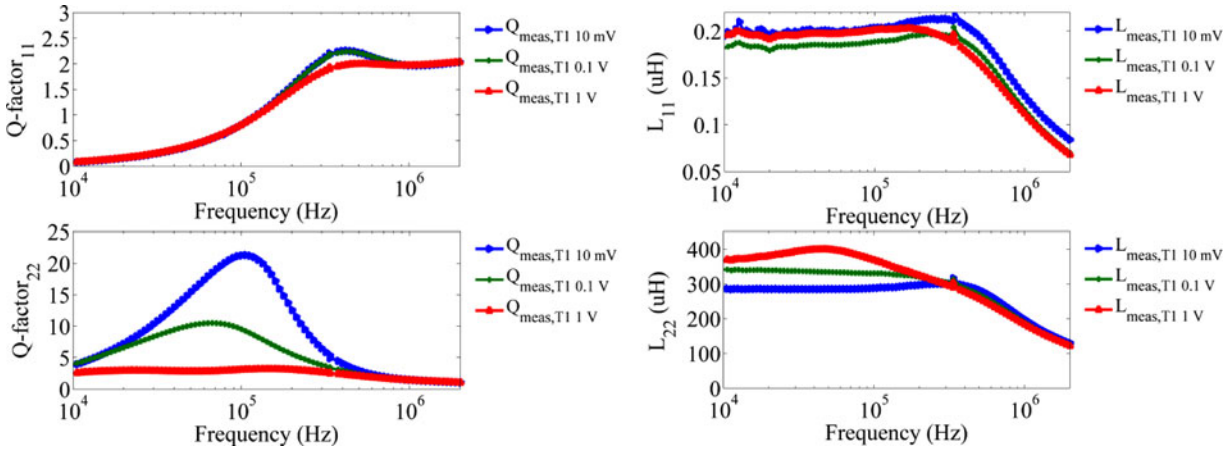

Fig. 12. Measured Q_{11}, Q_{22} (left) and L_{11}, L_{22} (right) for different ac voltage levels of the device with MnZn 75 core for T_1 layout.

$C_1 = 100$ nF, a coupling capacitor $C_2 = 1.3$ nF, and an output capacitor $C_{\rm aux} = 4.7$ μF. The rectified output is measured on the $V_{\rm out}$ node, while the low-voltage TEG source is emulated with a dc voltage source $V_{\rm DC}$ and a series resistor $R_{\rm teg} \approx 0.4$ Ω. The parameters were chosen for matching the properties of a commercial CP14 module from Laird Technologies [37].

Experimental measurements (see Fig. 15 on the left) on the 2:35 bond wire device with MnZn N30 core show that the circuit starts oscillating from an input voltage down to $V_{\rm DC} \cong 260$ mV with an oscillation frequency of 0.58 MHz while providing a steady-state rectified output up to 2 V. Besides, measurements (see Fig. 15 on the right) on the 1:10 Coilcraft transformer show that the circuit begins fluctuating from an input voltage down to $V_{\rm DC} \cong 200$ mV with an oscillation frequency of 0.53 MHz while providing a rectified output up to 2 V. The startup voltage difference is due to the higher L_{11}/R_{11} ratio of the Coilcraft component with respect to the bond wire device; however, the behavior is similar, thus confirming the bond wire transformer, which can be potentially implemented directly on-top-of an IC as in [17].

As a comparison, the proposed transformers have (at 0.1 MHz) a self-inductance up to $L_{11} \cong 1$ μH (see Table IV)

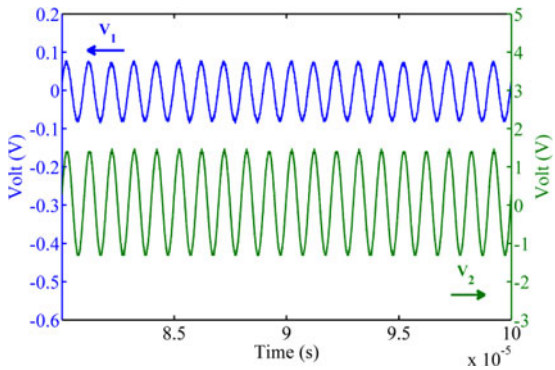

Fig. 13. Measured primary V_1 and secondary V_2 voltages of the MnZn N30 core with T_2 layout (1:33).

and a Q_{22}-factor of $\cong$10 (at 0.1 V rms from Fig. 12 on the left) in an area of $\cong$24 mm^2, with on-chip integration and lower profile achievable. Besides, commercial solutions (e.g., [35], [36]) provide similar or superior performance only with higher volumes. For instance, the 1:10 transformer in [35] has (at 0.1 MHz and 0.1 V rms) an $L_{11} \cong 25$ μH (25 times greater) and a Q_{22}-factor of $\cong$80 (eight times greater) in an area of $\cong$36 mm^2

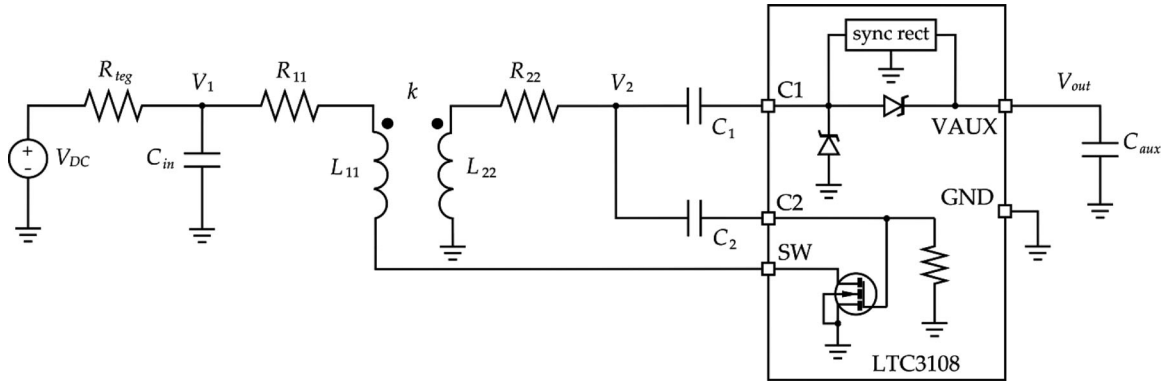

Fig. 14. Circuit diagram of the low-voltage step-up oscillator based on the LTC3108 IC with the microtransformer. The $V_{\rm out}$ pin represents the output of the internal rectifier connected to the step-up oscillator which is our main output.

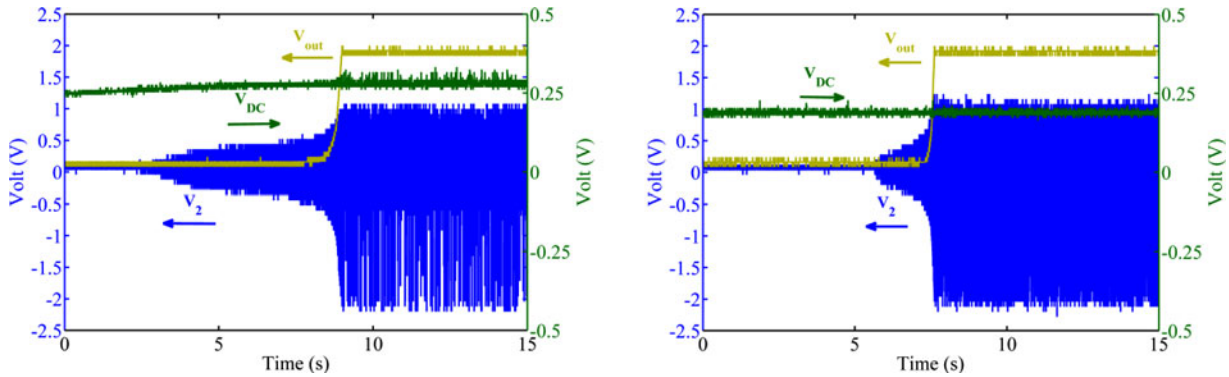

Fig. 15. Experimental waveforms: source $V_{\rm DC}$, secondary winding V_2, and rectified output $V_{\rm out}$ voltages with 2:35 bond wire MnZn N30 core (left) and with 1:10 Coilcraft (right) transformers. V_2 and $V_{\rm out}$ are referred to the left y-axis and $V_{\rm DC}$ to the right y-axis.

(1.5 times greater), whereas the 1:10 transformer in [36] has (at 0.1 MHz and 0.1 V rms) an $L_{11} \cong 2\ \mu$H (two times greater) and nearly same Q_{22}-factor of $\cong$11 in a lower area of $\cong$16 mm^2. However, the latter has a profile of 1.1 mm higher than the $\approx$0.6 mm of the bond wire magnetics. In addition, the bond wire transformers present a maximum dc inductance to resistance ratio of $\cong$70 μH/Ω and a maximum inductance per unit area of $\cong$12.8 μH/mm^2 up to 0.3 MHz.

VI. Conclusion

This study has investigated the design of bond wire micromagnetics to be used in low input voltage step-up oscillators as building blocks of EH systems. This technology is suitable for package and die level integrations. Several prototypes of bond wire transformers with gold IC bonding wires and high-permeability ferrite cores have been modeled and designed in order to get high inductance and high turns ratio in a fixed footprint area. The devices have been fabricated on a PCB substrate with different layouts and assembled based on manufacturable and repeatable wire bonding technology. However, the proposed process is also suitable for integration on-top of silicon ICs. Small-signal measurements demonstrate that the use of the ferrites compared to air-core increases inductance up to 315 μH with low dc series resistance and improves the coupling coefficient up to 0.9 with an effective turns ratio of 34. This represents one of the highest values for state-of-the-art toroidal magnetics. Small-signal measurements also report a peak secondary quality factor of 24.5 at 0.1 MHz. The presented design is cost effective and enables the development of inductors and transformers with adjustable performance. This makes in perspective the evolution of PwrSiP and PwrSoC possible with reliable efficient magnetics compatible with IC designs, provided that a full optimization of design parameters is performed.

A resonant low-voltage step-up oscillator for TEG sources has been realized based on a LTC3108 IC and the MnZn N30 device with 2:35 turns as step-up transformer. Experimental measurements on a discrete prototype report that the circuit starts oscillating from a voltage down to 260 mV with an oscillation frequency of 0.58 MHz and rectified output voltage of 2 V. This startup performance is comparable with that obtained with similar external components. Hence, the proposed bond wire micromagnetics can find use as on-top-of-chip components in bootstrap circuits for micropower EH applications whenever great size reductions are necessary.

Acknowledgment

The authors would like to thank F. Waldron and K. Rodgers of Tyndall National Institute for their valuable suggestions, and

P. Tassie and N. Nudds of Tyndall National Institute for bonding training and support.

REFERENCES

[1] C. O. Mathúna, N. Wang, S. Kulkarni, and S. Roy, "Review of integrated magnetics for power supply on chip (PwrSoC)," *IEEE Trans. Power Electron.*, vol. 27, no. 11, pp. 4799–4816, Nov. 2012.

[2] J.-P. Im, S.-W. Wang, S.-T. Ryu, and G.-H. Cho, "A 40 mV Transformer-reuse self-startup boost converter with MPPT control for thermoelectric energy harvesting," *IEEE J. Solid-State Circuits*, vol. 47, no. 12, pp. 3055–3067, Dec. 2012.

[3] P.-S. Weng, H.-Y. Tang, P.-C. Ku, and L.-H. Lu, "50 mV-Input batteryless boost converter for thermal energy harvesting," *IEEE J. Solid-State Circuits*, vol. 48, no. 4, pp. 1031–1041, Apr. 2013.

[4] C. R. Sullivan, D. V. Harburg, J. Qiu, C. G. Levey, and D. Yao, "Integrating magnetics for on-chip power: A perspective," *IEEE Trans. Power Electron.*, vol. 28, no. 9, pp. 4342–4353, Sep. 2013.

[5] D. J. Perreault, J. Hu, J. M. Rivas, Y. Han, O. Leitermann, R. C. N. Pilawa-Podgurski, A. Sagneri, and C. R. Sullivan, "Opportunities and challenges in very high frequency power conversion," in *Proc. Appl. Power Electron. Conf.*, Feb. 2009, pp. 1–14.

[6] D. Flynn, R. S. Dhariwal, and M. P. Y. Desmulliez, "A design study of microscale magnetic components for operation in the MHz frequency range," *J. Micromech. Microeng.*, vol. 16, pp. 1811–1818, 2006.

[7] M. Brunet, T. O'Donnell, L. Baud, N. Wang, J. O'Brien, P. McCloskey, and S. C. O'Mathuna, "Electrical performance of microtransformers for DC-DC converter applications," *IEEE Trans. Magn.*, vol. 38, no. 5, pp. 3174–3176, Sep. 2002.

[8] T. O'Donnell, N. Wang, R. Meere, F. Rhen, S. Roy, D. O'Sullivan, and C. O'Mathuna, "Microfabricated inductors for 20 MHz Dc-Dc converters," in *Proc. Appl. Power Electron. Conf.*, Feb. 2008, pp. 689–693.

[9] B. Orlando, R. Hida, R. Cuchet, M. Audoin, B. Viala, D. Pellissier-Tanon, X. Gagnard, and P. Ancey, "Low-resistance integrated toroidal inductor for power management," *IEEE Trans. Magn.*, vol. 42, no. 10, pp. 3374–3376, Oct. 2006.

[10] D. W. Lee, K-P. Hwang, and S. X. Wang, "Fabrication and analysis of high-performance integrated solenoid inductor with magnetic core," *IEEE Trans. Magn.*, vol. 44, no. 11, pp. 4089–4095, Nov. 2008.

[11] D. S. Gardner, G. Schrom, P. Hazucha, F. Paillet, T. Karnik, S. Borkar, R. Hallstein, T. Dambrauskas, C. Hill, C. Linde, W. Worwag, R. Baresel, and S. Muthukumar, "Integrated on-chip inductors using magnetic material (invited)," *J. Appl. Phys.*, vol. 103, no. 7, pp. 07E927-1–07E927-6, Apr. 2008.

[12] R. Meere, N. Wang, T. O'Donnell, S. Kulkarni, S. Roy, and S. C. O'Mathuna, "Magnetic-core and air-core inductors on silicon: a performance comparison up to 100 MHz," *IEEE Trans. Magn.*, vol. 47, no. 10, pp. 4429–4432, Oct. 2011.

[13] Q. Li, M. Lim, J. Sun, A. Ball, Y. Ying, F. C. Lee, and K. D. T. Ngo, "Technology roadmap for high frequency integrated DC-DC converter," in *Proc. Power Electron. Motion Control Conf.*, May 2009, pp. 1–8.

[14] J. Lu, H. Jia, A. Arias, X. Gong, and Z. J. Shen, "On-chip bondwire transformers for power SOC applications," in *Proc. Appl. Power Electron. Conf.*, Feb. 2008, pp. 199–204.

[15] J. Lu., Jia, X. Wang, K. Padmanabhan, W. G. Hurley, and Z. J. Shen, "Modeling, design, and characterization of multiturn bondwire inductors with ferrite epoxy glob cores for power supply system-on-chip or system-in-package applications," *IEEE Trans. Power Electron.*, vol. 25, no. 8, pp. 2010–2017, Aug. 2010.

[16] H. Jia, J. Lu, X. Wang, K. Padmanabhan, and Z. J. Shen, "Integration of a monolithic buck converter power IC and bondwire inductors with ferrite epoxy glob cores," *IEEE Trans. Power Electron.*, vol. 26, no. 6, pp. 1627–1630, Jun. 2011.

[17] E. Macrelli, A. Romani, N. Wang, S. Roy, M. Hayes, R. P. Paganelli, and M. Tartagni, "Design and fabrication of a 29 μH bondwire microtransformer with LTCC magnetic core on silicon for energy harvesting applications," in *Proc. Eurosensors Conf.*, pp. 1–4, Sep. 2014.

[18] E. Macrelli, N. Wang, S. Roy, M. Hayes, R. P. Paganelli, M. Tartagni, and A. Romani, "Design and fabrication of a 315 μH bondwire micro-transformer for ultra-low voltage energy harvesting," in *Proc. Design, Autom. Test Eur. Conf.*, Mar. 2014, pp. 1–4.

[19] J. J. Wang, "Flexible on-chip inductors and transformer," in *Proc. IMAPS Device Packag. Conf.*, Mar. 2010, pp. 1–5.

[20] C. R. Sullivan, W. Li, S. Prabhakaran, and L. Shanshan, "Design and fabrication of low-loss toroidal air-core inductors," in *Proc. IEEE Power Electron. Spec. Conf.*, Jun. 2007, pp. 1754–1759.

[21] P. N. Murgatroyd, "The optimal form for coreless inductors," *IEEE Trans. Magn.*, vol. 25, no. 3, pp. 2670–2677, May 1989.

[22] X. Yu, M. Kim, F. Herrault, C.-H. Ji, J. Kim, and M. G. Allen, "Silicon-embedded 3D toroidal air-core inductor with through-wafer interconnect for on-chip integration," in *Proc. IEEE 25th Int. Conf. Micro Electron. Mech. Syst.*, Feb. 2012, pp. 325–329.

[23] M. K. Kazimierczuk, *High-Frequency Magnetic Components*. New York, NY, USA: Wiley, 2009, chs. 1–2, 7, 8, 11.

[24] W. H. Preece, "On the heating effects of electric currents," *Proc. Royal Society of London*, vol. 36, nos. 228–231, pp. 464–471, 1883.

[25] G. G. Harman, *Wire Bonding in Microelectronics*, 3rd ed. New York, NY, USA: McGraw-Hill Professional, 2010, ch. 2.

[26] *Electronic Materials Handbook: Packaging, Volume I*. Materials Park, OH, USA: ASM Int., 1989.

[27] C. Harper, *Electronic Packaging and Interconnection Handbook*, 4th ed. New York, NY, USA: McGraw-Hill Professional, 2004, chs. 6–8.

[28] *The Impedance Measurement Handbook—Application Note*, 4th ed. Santa Clara, CA, USA: Agilent Technol., 2013, ch. 5.

[29] J. G. Hayes, D. Cashman, M. G. Egan, T. O'Donnell, and N. Wang, "Comparison of test methods for characterization of high-leakage two-winding transformers," *IEEE Trans. Ind. Appl.*, vol. 45, no. 5, pp. 1729–1741, Sep./Oct. 2009.

[30] Y. Han, G. Cheung, A. Li, C. R. Sullivan, D. J. Perreault, "Evaluation of magnetic materials for very high frequency power applications," *IEEE Trans. Power Electron.*, vol. 27, no. 1, pp. 425–435, Jan. 2012.

[31] H. Bottner, J. Nurnus, A. Schubert, and F. Volkert, "New high density micro structured thermogenerators for stand alone sensor systems," in *Proc. 26th Int. Conf. Thermoelectrics*, 2007, pp. 306–309.

[32] J. M. Damaschke, "Design of a low-input-voltage converter for thermoelectric generator," *IEEE Trans. Ind. Appl.*, vol. 33, no. 5, pp. 1203–1207, Sep./Oct. 1997.

[33] Y. K. Ramadass and A. P. Chandrakasan, "A battery-less thermoelectric energy harvesting interface circuit with 35 mV startup voltage," *IEEE J. Solid-State Circuits*, vol. 46, no. 1, pp. 333–341, Jan. 2011.

[34] Linear Technology. *Ultralow Voltage Step-Up Converter and Power Manager—LTC3108*. 2010. [Online]. Available: http://cds.linear.com/docs/en/datasheet/3108fc.pdf

[35] Coilcraft. *Miniature Step-Up Flyback Transformers—LPR6235*. 2010. [Online]. Available: http://www.coilcraft.com/pdfs/lpr6235.pdf

[36] Coilcraft. *Miniature Step-Up Flyback Transformers—LPR4012*. 2010. [Online]. Available: http://www.coilcraft.com/pdfs/lpr4012.pdf

[37] Laird Technologies. *CP Series CP14,31,045 Thermoelectric Modules.* 2013. [Online]. Available: http://www.lairdtech.com/products/thermal-management-solutions/thermoelectric-modules/#.UxCg5YXIkoc

Enrico Macrelli received the B.S. and M.S. degrees in electronic and telecommunications engineering, in 2007 and 2009, respectively, and the Ph.D. degree in information technology, in 2014, all from the University of Bologna, Bologna, Italy.

In 2012, he joined the Tyndall National Institute, Cork, Ireland, in the Nanofunction-WP2 project and worked on design and fabrication of magnetic materials and components. His research interests include design techniques for micropower energy harvesting systems and acoustic sensors.

Aldo Romani received the Dr.Eng. degree in electrical engineering and the Ph.D. degree in electrical engineering, computer science, and telecommunications from the University of Bologna, Bologna, Italy, in 2001 and 2005, respectively.

In 2008, he joined the University of Bologna, Cesena, Italy, as an Assistant Professor. He has authored or coauthored more than 35 international scientific publications. He has been involved with CMOS integrated sensors, applications of piezoelectric materials, and energy harvesting systems.

Dr. Romani was a corecipient of the 2004 Jan Van Vessem Award of the IEEE International Solid-State Circuits Conference.

Ningning Wang (M'12) received the B.S.E.E. and M.Sc. degrees in electrical engineering from Xi'an Jiaotong University, Xi'an, China, in 1995 and 1998, respectively, and the Ph.D. degree in the area of integrated magnetics for power conversion applications from University College Cork, Cork, Ireland, in 2005.

He joined the Tyndall National Institute, Cork, as a Postdoctoral Researcher in 2005 and was appointed as a Staff Researcher in early 2008. He has extensive research experience in design, modeling, and fabrication of integrated magnetics for power conversion and energy harvesting for wireless sensor network applications. He has participated and managed a number of research projects supported by national funding agencies, EU research funds, and industrial partners in domain of integrated magnetics for power conversion applications and energy harvesting-based power management. So far, he has published more than 70 papers in peer-reviewed Journals and conference proceedings in the area of integrated magnetic and power management.

Saibal Roy received the M.Sc. degree in physics from the Indian Institute of Technology, India, and the Ph.D. degree in advanced nanostructured materials from the Indian Association for the Cultivation of Science, Kolkata, India.

He is currently Head of Group within Microsystems Centre of Tyndall National Institute, Ireland. He is Science Foundation Ireland Principal Investigator (SFI PI) in the Micropower - Nanomagnetics research area. Since receiving Ph.D., his professional experiences include 17 years academic and 3 years industrial experiences. His current research interests at Tyndall include how engineered nanostructures could be employed for the benefits of micrometer-scale devices from More than Moore to beyond Moore scenario. Since joining the Tyndall Institute, he was able to bring substantial ($>$ € 6 Million) government and corporate competitive research grants. Some of his published work featured widely in media. He has supervised several ($\sim$25) Bachelors/Masters/Ph.D./Postdocs at EE/Microelectronics/Physics/Materials- Chemistry Departments of UCC/Tyndall. He has delivered invited talks in several international forums, has granted 2 international patents, written 7 book chapters, and over 140 papers in esteemed journals and peer-reviewed conference proceedings with a current h index of 25.

Dr. Roy has been honored by the President of University College Cork (UCC) for licensing a patented technology to INTEL.

Mike Hayes received the M.Eng.Sc. degree from the University College Cork, Cork, Ireland, in 1987.

In 2008, he brought over 20 years electronics technical & managerial experience to Tyndall as industry-led Program Manager for ICT enabled technologies for energy efficiency applications. This includes development of wireless sensor network platforms, energy harvesting systems, and conditional monitoring solutions & power electronics for EU, Irish, & industry partners. He is a work package leader on several EU projects (MOSYCOUSIS ARTEMIS ME3Gas, GreenCom) and coordinates IERC project ROWBUST (www.ierc.ie) developing energy harvesting, quality of service, and autocommissioning and return on investment models for wireless sensors.

Rudi Paolo Paganelli received the Dr.Eng. degree in electrical engineering, in 1998, and the Ph.D. degree in electrical engineering, computer science and telecommunications, in 2002, from the University of Bologna, Bologna, Italy.

In 2002, he joined the CNR-IEIIT in Bologna as a Research Fellow, and since 2003, he has been an Assistant Professor for the course of power electronics at the University of Bologna. His research interests include electronic device modeling, design techniques for microwave circuits, nonlinear circuits, and power electronics.

Cian Ó Mathúna (M'06–SM'11–F'13) received the B.E., M.Eng.Sc., and Ph.D. degrees from the National University of Ireland, Cork, Ireland, in 1981, 1984, and 1994, respectively.

He is currently the Head of the Microsystems Centre at the Tyndall National Institute, University College Cork, Cork. With a compliment of more than 80 researchers, and an annual budget of € 4.5m, the Centre incorporates two research groups: Microelectronics Applications Integration and Life Sciences Interface. His research interests include functional integration of electronic components such as sensors, actuators, power, and cooling. He is currently undertaking research on magnetics on silicon, energy harvesting, and wireless sensor networks for energy, health, and the environment.

Dr. Mathúna was the Director of the Power Sources Manufacturers Association (PSMA) from 2006 to 2010, and in 2008, he championed the First International Workshop on Power Supply on Chip. The workshop has been held in San Francisco, CA, USA, in November 2012, and is now cosponsored by the IEEE Power Electronics Society and the PSMA.

Marco Tartagni (M'99) received the M.S. degree in electrical engineering in 1988 and the Ph.D. degree in electrical engineering and computer Sciences in 1993 both from the University of Bologna, Bologna, Italy.

In 1994, he joined the Department of Electrical Engineering, California Institute of Technology, Pasadena, CA, USA, as a Research Fellow. Since March 1995, he has been with the Department of Electronics, University of Bologna, where he is currently an Associate Professor. In 1997, he designed the first silicon-only fingerprint capacitive sensor. In 1999, he co-founded the company Silicon Biosystems active in the field of lab-on-a-chip devices. From 2005 to 2008, he was an European coordinator of FP6 Receptronics in the Nanotechnology thematic area. Since 2008, he has been a coordinator of the Working Group on Energy Autonomous Systems within the European CATRENE initiative. Since 2014, he has been a Member of the Scientific Board and Team Leader of the joint STMicroelectronics and Bologna University lab for sensor design. He has coauthored more than 100 refereed scientific publications, 18 granted U.S. patents, and 11 European and WIPO patents

Prof. Tartagni was a co-recipient of the 2004 Jan Van Vessem Award of the IEEE International Solid-State Circuits Conference.